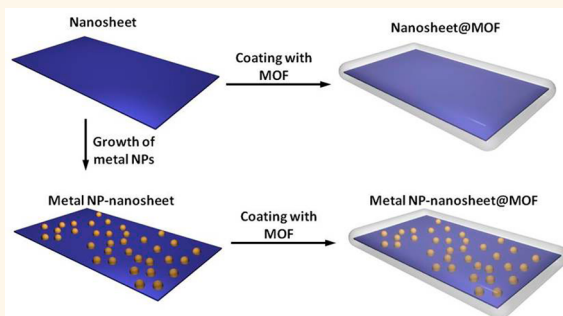


Coating Two-Dimensional Nanomaterials with Metal–Organic Frameworks

Xiao Huang,^{†,||} Bing Zheng,^{†,||} Zhengdong Liu,^{†,‡,||} Chaoliang Tan,[†] Juqing Liu,[†] Bo Chen,[†] Hai Li,[†] Junze Chen,[†] Xiao Zhang,[†] Zhanxi Fan,[†] Weina Zhang,[†] Zhen Guo,[§] Fengwei Huo,[†] Yanhui Yang,[§] Ling-Hai Xie,[‡] Wei Huang,^{‡,†} and Hua Zhang^{†,*}

[†]School of Materials Science and Engineering, Nanyang Technological University, 50 Nanyang Avenue, Singapore 639798, Singapore, [‡]Center for Molecular Systems and Organic Devices (CMSOD), Key Laboratory for Organic Electronics & Information Displays (KLOEID), Institute of Advanced Materials (IAM), Nanjing University of Posts & Telecommunications, 9 Wenyuan Road, Nanjing 210046, China, [§]School of Chemical and Biomedical Engineering, Nanyang Technological University, 62 Nanyang Drive, Singapore 637459, Singapore, and ^{||}Singapore-Jiangsu Joint Research Center for Organic/Bio-Electronics and Information Displays, Institute of Advanced Materials (IAM), Nanjing Tech University, Nanjing 211816, China. ^{||}These authors contributed equally to this work.

ABSTRACT We demonstrate the coating of various 2D nanomaterials including MoS₂ nanosheets, graphene oxide (GO), and reduced graphene oxide (rGO) with zeolitic imidazolate frameworks (*i.e.*, ZIF-8) *via* a facile procedure. Additionally, ternary core–shell structures like Pt-MoS₂@ZIF-8, Pt-GO@ZIF-8, and Pt-rGO@ZIF-8 have also been prepared. As a proof-of-concept application, a memory device based on MoS₂@ZIF-8 hybrid was fabricated and it exhibited write-once-read-many-times (WORM) memory effect with high ON/OFF ratio and long operating lifetime. It is expected that MOF coated 2D nanomaterials may find wide applications in energy storage and conversion, catalysis, sensing, and information storage devices.



KEYWORDS: 2D nanomaterials · MoS₂ · graphene · metal organic frameworks · hybrid nanomaterials · memory devices

Two-dimensional (2D) nanomaterials such as graphene and transition metal dichalcogenide (TMD) nanosheets have been the focus of recent research owing to their novel properties, which have made them appealing candidates in many applications, including electronic devices, catalysis, energy storage and conversion, and so on.^{1–6} Their hybridization with various nanostructures such as metals, metal oxides, and metal chalcogenides has proven effective in achieving improved properties and creation of novel functions.^{7–10}

As a unique class of ordered porous solids, metal organic frameworks (MOFs) or porous coordination polymers (PCPs) have received much attention over the past two decades.^{11–14} Compared to the other traditional porous materials (*e.g.*, porous carbon, mesoporous silica, and zeolite), MOFs possess a number of advantages such as rich surface chemistry, structural versatility, and tunable pore size in the nanometer regime.^{15–19} It can be imagined that embedding 2D nanomaterials

and their hybrids in MOF materials can further broaden their potential applications. Although several recent reports have demonstrated the hybridization of MOFs with graphene-based nanosheets,^{20–26} in most cases, graphene nanosheets were randomly distributed inside microsize MOF crystals,²³ or served as synthetic support for the surface decoration of dispersed MOF nanocrystals.^{24,25} The encapsulation of other types of 2D nanomaterials and their related composites in MOF matrices to form 2D core–shell structures, unfortunately, has not been realized. Herein, we demonstrate the coating of various 2D materials including MoS₂, graphene oxide (GO), and reduced graphene oxide (rGO) nanosheets, as well as their hybrids with metal nanoparticles (*i.e.*, Pt-MoS₂, Pt-GO, and Pt-rGO) with MOFs (*i.e.*, ZIF-8 used here). As a proof of concept, the memory device based on MoS₂@ZIF-8 hybrid has been investigated, which exhibits the write-once-read-many-times (WORM) memory effect with high ON/OFF ratio and long operating lifetime.

* Address correspondence to
HZhang@ntu.edu.sg,
hzhang166@yahoo.com.

Received for review July 13, 2014
and accepted July 30, 2014.

Published online July 30, 2014
10.1021/nn503834u

© 2014 American Chemical Society

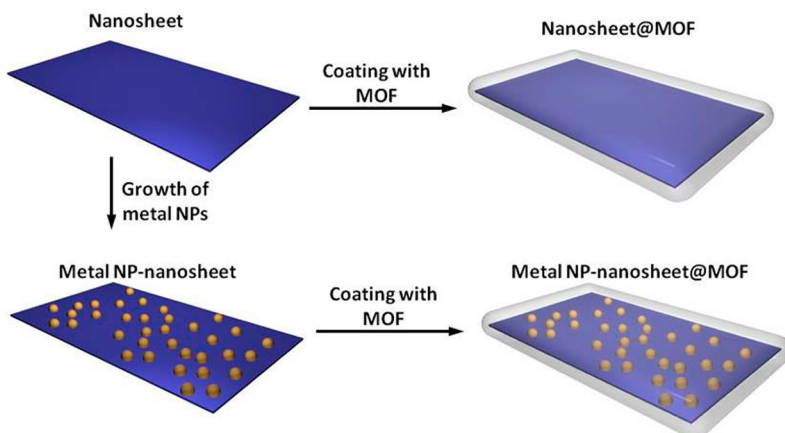


Figure 1. Schematic illustration of the formation process of nanosheet@MOF and metal NP–nanosheet@MOF hybrid structures.

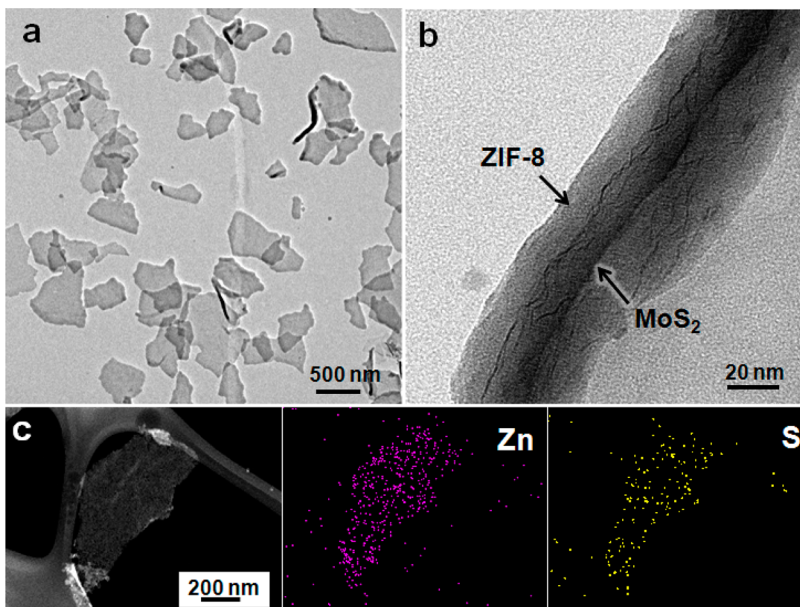


Figure 2. (a) TEM image of MoS_2 @ZIF-8 hybrid structures. (b) TEM image of a curled MoS_2 @ZIF-8 structure, showing the MoS_2 nanosheet and ZIF-8 coating. (c) STEM image and the corresponding EDS mapping of a typical MoS_2 @ZIF-8 hybrid structure.

RESULTS AND DISCUSSION

Figure 1 schematically shows the coating of 2D nanosheets and metal nanoparticle (NP)–nanosheet composite with MOFs. For example, MoS_2 nanosheets and Pt– MoS_2 composite (Figure S1 in the Supporting Information) were prepared by our previously developed methods,^{8,27} and then used as 2D template for the surface coating of ZIF-8 (see Methods and Materials for the detailed experimental procedure). Briefly, aqueous solutions of 2-methylimidazole (MIM, $\text{C}_4\text{H}_6\text{N}_2$) and zinc acetate ($\text{Zn}(\text{CH}_3\text{COO})_2 \cdot 2\text{H}_2\text{O}$) were mixed at ambient conditions in the presence of the aforementioned 2D templates with mild shaking. The mixture was then left undisturbed for 2 h before centrifugation, washing, and vacuum drying. The successful coating of ZIF-8 on MoS_2 and Pt– MoS_2 to form core–shell structures, *i.e.*, MoS_2 @ZIF-8 and Pt– MoS_2 @ZIF-8, respectively, was indicated by transmission electron microscopy

(TEM) and X-ray diffraction (XRD) analysis as shown in Figures 2 and 3, and Figures S2 and S3 in Supporting Information. For example, Figure 2a shows the TEM image of as-prepared MoS_2 @ZIF-8 hybrid structures. The TEM image of a curled MoS_2 @ZIF-8 hybrid reveals its cross section, which shows the embedded MoS_2 core and ZIF-8 shell (Figure 2b). The crystal structure of the coating was confirmed by XRD as ZIF-8 with cubic structure, space group $\bar{I}\bar{4}3m$ (Figure S2 in Supporting Information).²⁸ No specific orientation was observed in the XRD pattern, indicating the polycrystalline nature of the coated ZIF-8 shell. Note that the characteristic XRD peak for $\text{MoS}_2(002)$ at $\sim 15^\circ$ was not shown because the embedded MoS_2 nanosheets are too thin (*i.e.*, single to a few layers) to give detectable signal.²⁷ The scanning transmission electron microscope (STEM) image and the corresponding energy dispersive X-ray spectrometry (EDS) elemental mapping of a typical

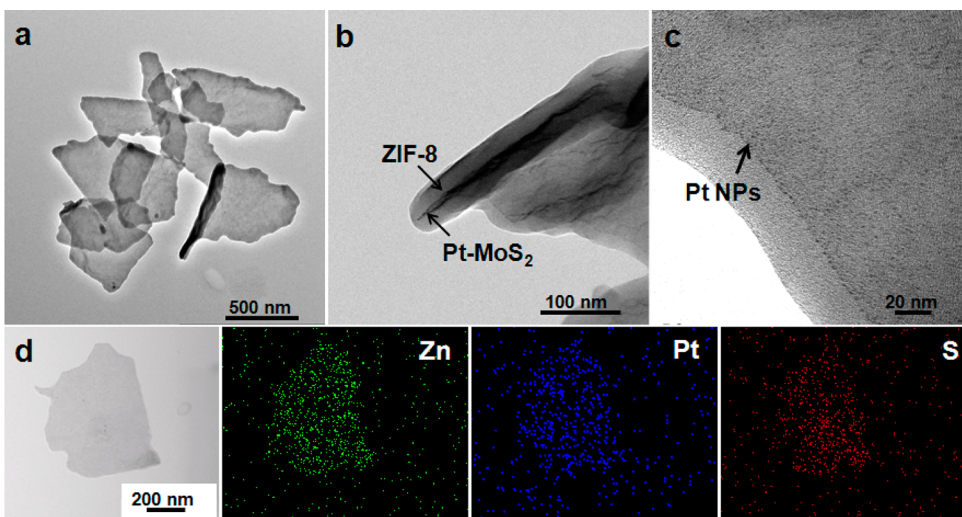


Figure 3. (a) TEM image of Pt-MoS₂@ZIF-8 hybrid structures. (b) TEM image of a curled Pt-MoS₂@ZIF-8 structure, showing the embedded Pt-MoS₂ core and ZIF-8 shell. (c) TEM image of the edge area of a Pt-MoS₂@ZIF-8 structure, revealing the embedded Pt NPs. (d) STEM image and the corresponding EDS mapping of a typical Pt-MoS₂@ZIF-8 hybrid structure.

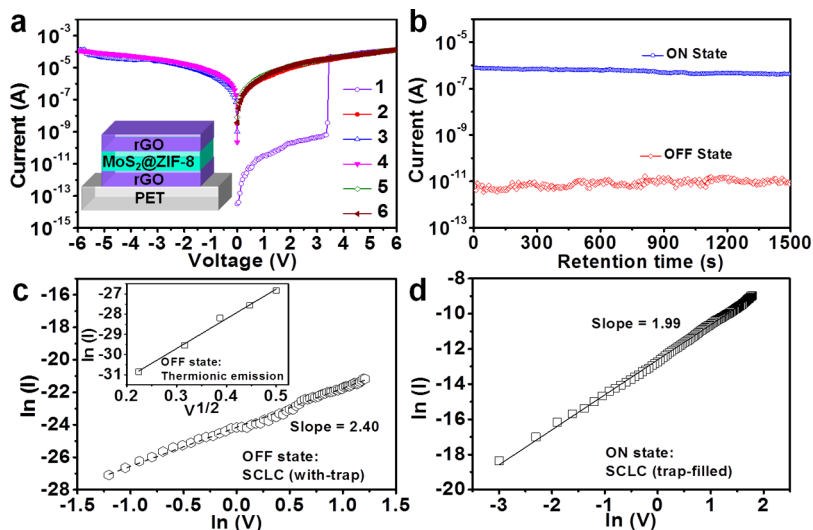


Figure 4. (a) The I – V characteristics of the MoS₂@ZIF-8 based flexible memory device. Inset: the schematic of the device. (b) The retention-ability test of the memory device at a reading voltage of 0.5 V in the ON and OFF states. Experimental data and fitted lines of the I – V characteristics in (c) the OFF state and (d) the ON state.

MoS₂@ZIF-8 structure shows the uniform distribution of Zn and S elements (Figure 2c). Note that the signal for Mo is not shown since its peak in the EDS spectrum is close to S. Similarly, Figure 3a shows the TEM image of as-prepared Pt-MoS₂@ZIF-8 hybrid structures. The TEM image of a curled Pt-MoS₂@ZIF-8 hybrid in Figure 3b clearly indicates that the Pt-MoS₂ nanosheet is covered by ZIF-8 on both sides. A magnified TEM image on the edge area of a Pt-MoS₂@ZIF-8 hybrid structure reveals the embedded Pt NPs (Figure 3c). STEM-EDS analysis further confirms the presence of Zn, Pt, and S elements in the Pt-MoS₂@ZIF-8 hybrid (Figure 3d).

As mentioned above, the hybridization of 2D materials with other functional species has led to the enhanced performance in various applications. As a

proof-of-concept demonstration, the electronic property and switching effect of MoS₂@ZIF-8 based flexible memory device with the configuration of poly(ethylene terephthalate) (PET)/rGO/MoS₂@ZIF-8/rGO was investigated by current–voltage (I – V) characteristics (see Methods and Materials for the detailed fabrication process of the device). As shown in Figure 4a, the MoS₂@ZIF-8 based device exhibited bistable electrical behavior. Starting with the low conductivity state (OFF state) in the device, the current state increased abruptly from 7.0×10^{-10} to 5.0×10^{-5} A with the applied negative voltage increased to +3.3 V, indicating that the electrical property transformed to a high current state (ON state). The transition from the OFF state to the ON state serves as the “writing” process. In the subsequent positive sweep (stage 2), the device

remained in its high conductivity state, with an ON/OFF ratio of over 7.0×10^4 at 0.5 V. After a reverse sweep to -6.0 V (stage 3), the diode remained at the high conductivity state and did not recover its resistance to the OFF state (stage 4), indicating the inerasable data storage characteristic. Moreover, the high conductivity state still remained in stage 5, suggesting the WORM memory behavior of the $\text{MoS}_2@\text{ZIF-8}$ based device, which is different from the previously reported $\text{Ag}/\text{Rb-CD-MOF}/\text{Ag}$ memory (resistive random access memory, RRAM).²⁹ For comparison, the $I-V$ behavior of the pure rGO–rGO junction between two rGO electrodes was also measured (Figure S4 in Supporting Information), which showed higher current than the On-state current of the $\text{MoS}_2@\text{ZIF-8}$ based memory device after the electrical switching, indicating that a short circuit did not occur during the operation of the $\text{MoS}_2@\text{ZIF-8}$ based device. To explore the stability of our device, the retention time test was carried out in the ON and OFF states, respectively (Figure 4b). The ON and OFF states of the device did not undergo significant fluctuation even after more than 1.5×10^3 s of test under ambient conditions at a reading bias of $+0.5$ V. The long retention time indicates the highly stable information storage capability of our device.

To understand the carrier transport mechanism of the $\text{MoS}_2@\text{ZIF-8}$ based memory device, the experimental and fitted data of the $I-V$ curves were investigated (Figure 4c,d). In the OFF state, the plot of $\ln(I)$ vs $V^{1/2}$ from 0 to 0.3 V is fitted to a straight line (inset of Figure 4c). Such a linear characteristic indicates that the conduction mechanism probably arises from the thermionic emission,³⁰ and the charge injection from rGO electrode to $\text{MoS}_2@\text{ZIF-8}$ active layer is dominant.³¹ After that, a linear relation was observed in the plot of $\ln(I)$ vs $\ln(V)$ for the voltage sweep from 0.3 to 3.3 V, with a slope of 2.40 (larger than 2), suggesting that the trap-limited space-charge-limited-current (SCLC) dominated the carrier transport process.³² During this process, charges were transferred from ZIF-8 to MoS_2 , and then trapped by MoS_2 due to the lower energy level of MoS_2 compared to ZIF-8 and quantum confinement effect,³³ together with a lower free carrier density than the trap density induced by MoS_2 , resulting in the SCLC model with trap.³⁴ With a further increase in the bias, the traps were completely filled and the current increased exponentially, resulting in the trap-filled SCLC mechanism with a slope of 1.99 (nearly 2) in the ON state. The observed SCLC mode instead of ohmic behavior also indicates that a short circuit did not occur during the device operation.³⁵ Moreover, the trapped charges in MoS_2 were retained after the power was off, due to the insulting property of the ZIF-8 material used as encapsulation matrix, which enabled the high conductivity and nonvolatility of the memory device. When a reverse voltage was applied, the non-erasing behavior indicated that the trapped charges

could not be detrapped, which was probably due to the relatively thick shell of ZIF-8 (typically 20–30 nm, Figure 2b). Therefore, the device exhibited WORM memory effect.

In addition to MoS_2 nanosheets, by using our aforementioned general method, we have also successfully coated ZIF-8 on graphene-based materials, such as GO and rGO nanosheets, as well as their composites with Pt NPs, *i.e.*, Pt-GO and Pt-rGO (Figure S5 in Supporting Information). The detailed characterizations of GO@ZIF-8, rGO@ZIF-8, Pt-GO@ZIF-8, and Pt-rGO@ZIF-8 hybrid materials are shown in Figure 5, and Figures S6–S8 in Supporting Information. For example, Figure 5a shows the TEM image of the Pt-rGO@ZIF-8 hybrid structures. The magnified TEM image of a typical Pt-rGO@ZIF-8 hybrid material reveals the embedded 1–3 nm Pt NPs (Figure 5b). XRD pattern confirms the coated layer is ZIF-8 (Figure 5c). Note that the characteristic peak for stacked rGO sheets at $\sim 24^\circ$ (ref 36) is not observed because the coating of ZIF-8 enlarges the distance between adjacent rGO sheets. The thickness of the hybrid structure is ~ 80 nm based on the AFM measurement (Figure 5d). It is noteworthy that in our method, the organic ligand (*i.e.*, MIM as precursor for ZIF-8) was directly used as the surface capping and stabilizing agent for graphene-based materials during the deposition of ZIF-8 shell. This is a crucial step especially for deposition of ZIF-8 on rGO or Pt-rGO nanosheets, which show low solubility in polar solvents. For example, MIM was used to stabilize GO sheets or Pt-GO hybrid nanosheets when they were reduced by NaBH_4 in water. Note that the oxygen-containing groups on GO/rGO sheets will not react with MIM in water at ambient conditions. Therefore, MIM molecules were likely absorbed on graphene-based nanosheets *via* $\pi-\pi$ interaction.³⁷ Evidently, discontinuous islands of ZIF-8 were first formed on the surface of the nanosheets (Figure S9 in Supporting Information), and gradually grew into continuous shells. In addition, to confirm that our method can yield continuous coating of ZIF-8 on 2D materials, the obtained Pt-rGO@ZIF-8 hybrid material was used to selectively catalyze liquid-phase hydrogenation of *n*-hexene *versus* *cis*-cyclooctene,³⁸ which showed the conversion efficiency of 21% and 4.8%, respectively (Figure S10 in Supporting Information). It is worth noting that since the commercial *cis*-cyclooctene (95%, Aldrich) used here contains $\sim 3.1\%$ cyclooctane (Figure S11 in Supporting Information), the conversion efficiency of 4.8% toward *cis*-cyclooctene is in fact negligible. For comparison, the catalytic performance of Pt-rGO without MOF coating was also tested, which showed the conversion efficiency of 100% and 99% for hydrogenation of *n*-hexene and *cis*-cyclooctene, respectively (Figure S12 in Supporting Information). The superior selectivity of Pt-rGO@ZIF-8 compared to that of Pt-rGO may arise from the selective permeability of the continuous ZIF-8 coating,³⁸ which has a

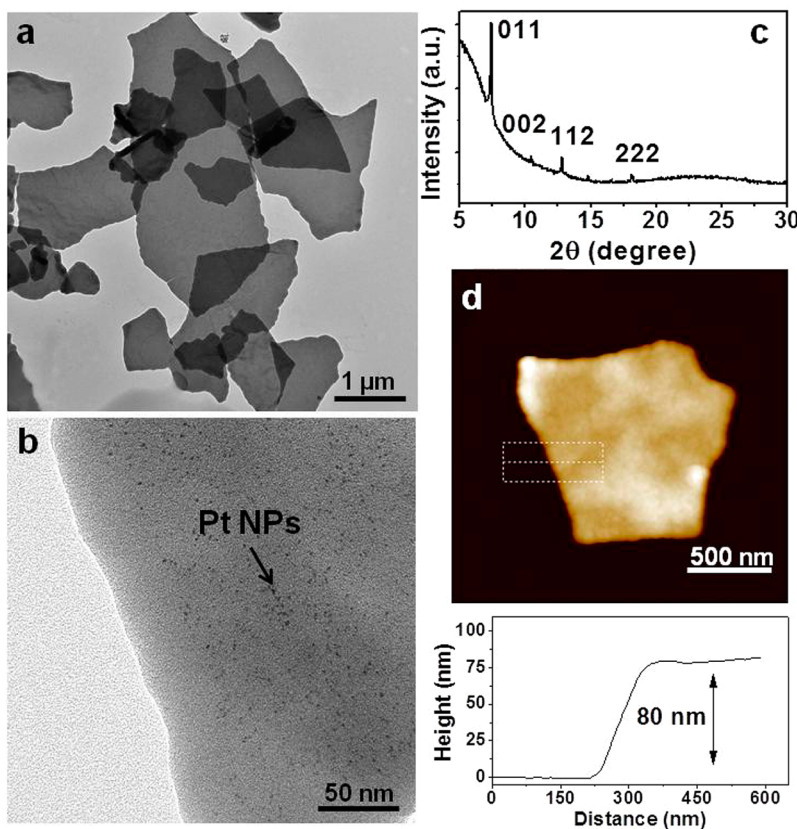


Figure 5. (a) TEM image of Pt-rGO@ZIF-8 hybrid nanostructures. (b) Magnified TEM image showing the embedded Pt NPs. (c) XRD pattern of as-prepared Pt-rGO@ZIF-8 hybrid nanostructures. (d) AFM image and height analysis of a typical Pt-rGO@ZIF-8 hybrid structure.

pore size of 3.4 \AA and thus can allow *n*-hexene molecules to pass through but block the steric *cis*-cyclooctene molecules. However, the conversion efficiency of Pt-rGO@ZIF-8 toward *n*-hexene is lower compared to that of Pt-rGO. This might be due to the reduced diffusion rate of *n*-hexene through the ZIF-8 layer.

CONCLUSION

In summary, we have demonstrated the coating of various 2D nanomaterials such as MoS₂, GO, and

rGO nanosheets, and their hybrids with metal NPs (*i.e.*, Pt-GO, Pt-rGO, and Pt-MoS₂) with ZIF-8. As a proof-of-concept application, we have also investigated the performance of MoS₂@ZIF-8 core–shell structure in memory device. It is believed that the formation of these 2D core–shell structures based on functional 2D materials as core and MOFs as shell will open up more opportunities for catalysis, energy storage and conversion, and information storage devices.

METHODS AND MATERIALS

Materials. *Chemicals.* Natural graphite (SP-1) was purchased from Bay Carbon (Bay City, MI) and used for synthesis of GO. Hydrogen chloride (fuming, 37%) and ethanol (99.9%, absolute) were purchased from Merck (Darmstadt, Germany). MoS₂ bulk crystals were purchased from Rose Mill (West Hartford, CT). Lithium-ion battery electrolyte was purchased from Charlston Technologies Pte Ltd. (International Business Park, Singapore). Lithium foil and copper foil were purchased from ACME Research Support Pte Ltd. (Bukit Batok Street, Singapore). Acetone (Tech grade) was purchased from Aik Moh Paints and Chemicals Pte Ltd. (Singapore). Potassium permanganate (KMnO₄), 98% H₂SO₄, poly(vinylidene fluoride) (PVDF), *N*-methylpyrrolidone (NMP), potassium tetrachloroplatinate(II) (99.99%), sodium borohydride (99.99%), zinc acetate (Zn(CH₃COO)₂·2H₂O), 2-methylimidazole (MIM, C₄H₆N₂), methanol (CH₃OH), ethyl acetate (99.8%), *n*-hexene (>99%), *cis*-cyclooctene (95%), and sodium citrate tribasic dehydrate (ACS reagent, 99.0%) were purchased

from Sigma-Aldrich (Steinheim, Germany). All chemicals were used as received without further purification. The deionized water was purified using Milli-Q System (Millipore, Billerica, MA) to produce Milli-Q water used for the following experiments.

Synthesis of Graphene Oxide (GO). All the glassware was washed by *aqua regia* (HNO₃/HCl = 1:3, v/v) and then rinsed by Milli-Q water at least twice (**Caution:** *aqua regia* is a quite strong oxidant and should be handled with great care). Single-layer GO sheets were synthesized from natural graphite by a modified Hummers method.³⁹ The as-prepared GO sheets were dispersed into ethanol or water with a concentration of 0.2 mg mL⁻¹ by sonication.

Preparation of Reduced Graphene Oxide (rGO). The preparation of rGO was based on the previous report.⁴⁰ Briefly, 1 mL of GO dispersion in water (0.2 mg mL⁻¹) was mixed with 9 mL of MIM aqueous solution (200 mM) in a glass vial under magnetic stirring for 2 h at room temperature. After that, the mixture in the glass vial was heated on a hot plate at 80 °C under magnetic

stirring, and 0.2 mL of fresh-prepared NaBH_4 aqueous solution (100 mM) was added to reduce GO. After 20 min, the resulting dark solution was centrifuged at 7500 rpm for 10 min, and the precipitate was redispersed in aqueous MIM solution (100 mM) for further use.

Preparation of MoS_2 Nanosheets. MoS_2 nanosheets were produced by the electrochemical intercalation and exfoliation method recently reported by our group.²⁷ The lithium intercalation was performed in a test cell using the Li foil as anode and 1 M LiPF_6 as electrolyte, which was dissolved in a mixture of ethyl carbonate (EC) and dimethyl carbonate (DMC) with a volume ratio of 1:1. The bulk MoS_2 powder (2 mg) mixed with acetylene black and poly(vinylidene fluoride) (PVDF) binder dispersed in *N*-methylpyrrolidone (NMP) was used as cathode. In the mixed slurry, the mass ratio of MoS_2 , acetylene black, and PVDF was 80:10:10. The resulting slurry was then uniformly coated on a copper foil and dried under vacuum overnight. The electrochemical intercalation of the layered materials in the test cell was accomplished in a Neware battery test system at room temperature. The electrochemical intercalation was performed using the galvanostatic discharge at current density of 0.025 mA. After the discharge process, the Li-intercalated sample (prepared from 2 mg MoS_2) was washed with acetone to remove any residual electrolyte (LiPF_6), followed by exfoliation and ultrasonication in 20 mL distilled water to obtain the 0.1 mg mL^{-1} MoS_2 solution.

Synthesis of Pt-GO and Pt- MoS_2 Hybrid Nanomaterials. After 2 mL of 0.05 mg mL^{-1} GO solution (or 0.1 mg mL^{-1} MoS_2 solution) was centrifuged at 8500 rpm for 20 min, the supernatant was removed and the precipitate was redispersed in 8 mL fresh growth solution containing 0.2 mM K_2PtCl_4 and 0.3 mM trisodium citrate in water. This mixed solution in a 10 mL glass vial was then irradiated with a 150 W halogen lamp at 80% of its full intensity for 2 h, during which the glass vial was cooled by ice water to prevent the light-induced overheating. After the reaction, the resulting solution was centrifuged at 7500 rpm for 15 min, and the precipitated Pt-GO or Pt- MoS_2 hybrid nanomaterials were redispersed in water before subsequent reactions.

Synthesis of Pt-rGO Hybrid Nanomaterials. After 5 mL of Pt-GO dispersion in water (0.02 mg mL^{-1}) was mixed with 5 mL of MIM aqueous solution (200 mM) in a glass vial under magnetic stirring for 2 h at room temperature, 0.25 mL of fresh-prepared NaBH_4 aqueous solution (100 mM) was added into the mixture to reduce GO. After 20 min, the resulting dark solution was centrifuged at 7500 rpm for 10 min, and the precipitate was redispersed in aqueous MIM solution (100 mM) for further use.

Coating ZIF-8 on 2D Nanomaterials. GO, rGO, Pt-GO, or Pt-rGO dispersion (0.1 mL, 0.2 mg mL^{-1}) in aqueous MIM (100 mM) solution, or MoS_2 dispersion (0.2 mL, 0.2 mg mL^{-1}) in aqueous MIM (100 mM) was mixed with 0.5 mL of water in a glass vial, followed by addition of freshly prepared aqueous solution of MIM (0.6 mL, 200 mM) and Zn(OAC)_2 (0.5 mL, 100 mM) in sequence with mild shaking. This mixture was allowed to react at room temperature for 2 h. After that, the resulting solution was centrifuged at 2500 rpm for 10 min and washed three times with methanol before drying in vacuum oven for further application. Note that rGO@ZIF-8 and Pt-rGO@ZIF-8 can also be prepared by reduction of presynthesized GO@ZIF-8 and Pt-GO@ZIF-8 in hydrazine vapor, respectively. To coat ZIF-8 on Pt- MoS_2 nanosheets, 0.2 mL of Pt- MoS_2 (0.2 mg mL^{-1}) dispersion in water was mixed with 0.5 mL of water in a glass vial, followed by addition of freshly prepared aqueous solution of Zn(OAC)_2 (0.5 mL, 100 mM) and MIM (0.6 mL, 200 mM) in sequence with mild shaking. Other experimental conditions were the same as those for coating ZIF-8 on MoS_2 .

Fabrication of Memory Device. After the fabrication of patterned rGO/PET electrodes,⁴¹ 0.2 mL of MoS_2 @ZIF-8 solution in CH_3OH was spin-coated onto the electrodes at 500 rpm for 10 s and then 3000 rpm for 50 s. The obtained MoS_2 @ZIF-8 film on rGO electrodes was dried at 60 °C for 12 h in vacuum oven. After that, patterned rGO/poly(methyl methacrylate) (PMMA) films were transferred onto MoS_2 @ZIF-8 layer, perpendicularly aligning to the bottom patterned rGO electrodes. Finally, PMMA was removed by acetone, and the prepared devices were dried at 60 °C in vacuum oven overnight for further characterization. The

electrical measurement was performed under ambient conditions by using a Keithley 4200 semiconductor parameter analyzer.

Catalytic Hydrogenation of Alkenes. Hydrogenation of alkenes (*i.e.*, *n*-hexene >99%, or *cis*-cyclooctene 95%) was carried out in ethyl acetate solution in a static hydrogen atmosphere (1 atm). In a typical experiment, the catalyst (based on the same amount of Pt) was loaded in a reactor and residual air in the reactor was expelled by flushing with hydrogen for several times. Ethyl acetate (2.0 mL) and alkene (*i.e.*, 0.1 mL *n*-hexene or *cis*-cyclooctene) were then added into the reactor in sequence. After the reactor was flushed with hydrogen once again, the reaction was allowed to proceed at 1 atm of hydrogen and 35 °C for 24 h. After the reaction, the catalyst powder was filtered, and the filtrate was analyzed using a gas chromatography (GC, Agilent, 6890N) equipped with a HP-5 column (Agilent) and a flame ionization detector (FID). It is worth noting that the commercial *cis*-cyclooctene (95%, Aldrich) contains ~3.1% cyclooctane as detected by GC (Figure S11 in Supporting Information).

Characterization. A drop of a solution containing the hybrid nanomaterials was placed on a holey carbon-coated copper grid, Si/SiO_2 and glass, and then naturally dried in air prior to characterization by transmission electron microscopy (TEM, JEM 2100F), X-ray photoelectron spectroscopy (XPS, Axis Ultra), and X-ray diffraction (XRD, Shimadzu), respectively.

Conflict of Interest: The authors declare no competing financial interest.

Supporting Information Available: TEM images and SAED patterns of as-prepared Pt- MoS_2 , Pt-GO and Pt-rGO hybrid structures; XRD patterns of as-prepared MoS_2 @ZIF-8 and Pt- MoS_2 @ZIF-8 hybrid structures; the current–voltage (*I*–*V*) characteristic of the pure rGO–rGO junction between two rGO electrodes; TEM images and XRD patterns of as-prepared GO@ZIF-8 rGO@ZIF-8 and Pt-GO@ZIF-8 hybrid materials; TEM image and XRD pattern of intermediate product obtained after rGO sheets in MIM solution reacted with zinc acetate for 10 min; GC spectra for calculation of the conversion efficiency of Pt-rGO and Pt-rGO@ZIF-8 toward hydrogenation of hexene versus *cis*-cyclooctene; GC spectrum of commercial *cis*-cyclooctene (95%, Aldrich), which contains 3.1% of *cis*-cyclooctane. This material is available free of charge via the Internet at <http://pubs.acs.org>.

Acknowledgment. This work was supported by Singapore MOE under AcRF Tier 2 (ARC 26/13, No. MOE2013-T2-1-034), AcRF Tier 1 (RG 61/12, RGT18/13, and RG5/13), and Start-Up Grant (M4080865.070.706022) in Singapore. This research is also conducted by NTU-HUJ-BGU Nanomaterials for Energy and Water Management Programme under the Campus for Research Excellence and Technological Enterprise (CREATE), that is supported by the National Research Foundation, Prime Minister's Office, Singapore.

REFERENCES AND NOTES

- Huang, X.; Qi, X. Y.; Boey, F.; Zhang, H. Graphene-Based Composites. *Chem. Soc. Rev.* **2012**, *41*, 666–686.
- Sun, Y.; Gao, S.; Xie, Y. Atomically-Thick Two-Dimensional Crystals: Electronic Structure Regulation and Energy Device Construction. *Chem. Soc. Rev.* **2014**, *43*, 530–546.
- Huang, X.; Zeng, Z. Y.; Zhang, H. Metal Dichalcogenide Nanosheets: Preparation, Properties and Applications. *Chem. Soc. Rev.* **2013**, *42*, 1934–1946.
- Sun, Y.; Cheng, H.; Gao, S.; Liu, Q.; Sun, Z.; Xiao, C.; Wu, C.; Wei, S.; Xie, Y. Atomically Thick Bismuth Selenide Free-standing Single Layers Achieving Enhanced Thermoelectric Energy Harvesting. *J. Am. Chem. Soc.* **2012**, *134* (50), 20294–20297.
- Xie, J.; Zhang, J.; Li, S.; Grote, F.; Zhang, X.; Zhang, H.; Wang, R.; Lei, Y.; Pan, B.; Xie, Y. Controllable Disorder Engineering in Oxygen-Incorporated MoS_2 Ultrathin Nanosheets for Efficient Hydrogen Evolution. *J. Am. Chem. Soc.* **2013**, *135*, 17881–17888.
- Sun, Y.; Cheng, H.; Gao, S.; Sun, Z.; Liu, Q.; Liu, Q.; Lei, F.; Yao, T.; He, J.; Wei, S.; Xie, Y. Freestanding Tin Disulfide Single-Layers Realizing Efficient Visible-Light Water Splitting. *Angew. Chem., Int. Ed.* **2012**, *51*, 8727–8731.

7. Machado, B. F.; Serp, P. Graphene-Based Materials for Catalysis. *Catal. Sci. Technol.* **2012**, *2*, 54–75.
8. Huang, X.; Zeng, Z. Y.; Bao, S. Y.; Wang, M. F.; Qi, X. Y.; Fan, Z. X.; Zhang, H. Solution-Phase Epitaxial Growth of Noble Metal Nanostructures on Dispersible Single-Layer Molybdenum Disulfide Nanosheets. *Nat. Commun.* **2013**, *4*, 1444.
9. Yoo, E.; Okata, T.; Akita, T.; Kohyama, M.; Nakamura, J.; Honma, I. Enhanced Electrocatalytic Activity of Pt Subnanoclusters on Graphene Nanosheet Surface. *Nano Lett.* **2009**, *9*, 2255–2259.
10. Huang, X.; Tan, C.; Yin, Z.; Zhang, H. 25th Anniversary Article: Hybrid Nanostructures Based on Two-Dimensional Nanomaterials. *Adv. Mater.* **2014**, *26*, 2185–2204.
11. Bureekaew, S.; Horike, S.; Higuchi, M.; Mizuno, M.; Kawamura, T.; Tanaka, D.; Yanai, N.; Kitagawa, S. One-Dimensional Imidazole Aggregate in Aluminium Porous Coordination Polymers with High Proton Conductivity. *Nat. Mater.* **2009**, *8*, 831–836.
12. Furukawa, H.; Ko, N.; Go, Y. B.; Aratani, N.; Choi, S. B.; Choi, E.; Yazaydin, A. O.; Snurr, R. Q.; O’Keeffe, M.; Kim, J.; et al. Ultrahigh Porosity in Metal-Organic Frameworks. *Science* **2010**, *329*, 424–428.
13. Reboul, J.; Furukawa, S.; Horike, N.; Tsotsalas, M.; Hirai, K.; Uehara, H.; Kondo, M.; Louvain, N.; Sakata, O.; Kitagawa, S. Mesoscopic Architectures of Porous Coordination Polymers Fabricated by Pseudomorphic Replication. *Nat. Mater.* **2012**, *11*, 717–723.
14. Zhou, H. C.; Long, J. R.; Yaghi, O. M. Introduction to Metal-Organic Frameworks. *Chem. Rev.* **2012**, *112*, 673–674.
15. Liu, Y.; Tang, Z. Multifunctional Nanoparticle@MOF Core–Shell Nanostructures. *Adv. Mater.* **2013**, *25*, 5819–5825.
16. He, L.; Liu, Y.; Liu, J.; Xiong, Y.; Zheng, J.; Liu, Y.; Tang, Z. Core–Shell Noble-Metal@Metal-Organic-Framework Nanoparticles with Highly Selective Sensing Property. *Angew. Chem., Int. Ed.* **2013**, *52*, 3741–3745.
17. Zhao, M.; Deng, K.; He, L.; Liu, Y.; Li, G.; Zhao, H.; Tang, Z. Core–Shell Palladium Nanoparticle@Metal–Organic Frameworks as Multifunctional Catalysts for Cascade Reactions. *J. Am. Chem. Soc.* **2014**, *136*, 1738–1741.
18. Stock, N.; Biswas, S. Synthesis of Metal-Organic Frameworks (MOFs): Routes to Various MOF Topologies, Morphologies, and Composites. *Chem. Rev.* **2012**, *112*, 933–969.
19. Cohen, S. M. Postsynthetic Methods for the Functionalization of Metal-Organic Frameworks. *Chem. Rev.* **2012**, *112*, 970–1000.
20. Jahan, M.; Liu, Z.; Loh, K. P. A Graphene Oxide and Copper-Centered Metal Organic Framework Composite as a Tri-Functional Catalyst for HER, OER, and ORR. *Adv. Funct. Mater.* **2013**, *23*, 5363–5372.
21. Jahan, M.; Bao, Q.; Loh, K. P. Electrocatalytically Active Graphene–Porphyrin MOF Composite for Oxygen Reduction Reaction. *J. Am. Chem. Soc.* **2012**, *134*, 6707–6713.
22. Jahan, M.; Bao, Q.; Yang, J.-X.; Loh, K. P. Structure-Directing Role of Graphene in the Synthesis of Metal-Organic Framework Nanowire. *J. Am. Chem. Soc.* **2010**, *132*, 14487–14495.
23. Petit, C.; Bandosz, T. J. MOF-Graphite Oxide Composites: Combining the Uniqueness of Graphene Layers and Metal-Organic Frameworks. *Adv. Mater.* **2009**, *21*, 4753–4757.
24. Kumar, R.; Jayaramulu, K.; Maji, T. K.; Rao, C. N. R. Hybrid Nanocomposites of ZIF-8 with Graphene Oxide Exhibiting Tunable Morphology, Significant CO₂ Uptake and Other Novel Properties. *Chem. Commun.* **2013**, *49*, 4947–4949.
25. Liu, S.; Sun, L. X.; Xu, F.; Zhang, J.; Jiao, C. L.; Li, F.; Li, Z. B.; Wang, S.; Wang, Z. Q.; Jiang, X.; et al. Nanosized Cu-MOFs Induced by Graphene Oxide and Enhanced Gas Storage Capacity. *Energy Environ. Sci.* **2013**, *6*, 818–823.
26. Kumar, R.; Jayaramulu, K.; Maji, T. K.; Rao, C. N. R. Growth of 2D Sheets of A MOF on Graphene Surfaces to Yield Composites with Novel Gas Adsorption Characteristics. *Dalton Trans.* **2014**, *43*, 7383–7386.
27. Zeng, Z. Y.; Yin, Z. Y.; Huang, X.; Li, H.; He, Q. Y.; Lu, G.; Boey, F.; Zhang, H. Single-Layer Semiconducting Nanosheets: High-Yield Preparation and Device Fabrication. *Angew. Chem., Int. Ed.* **2011**, *50*, 11093–11097.
28. Li, S.; Shi, W.; Lu, G.; Li, S.; Loo, S. C. J.; Huo, F. Unconventional Nucleation and Oriented Growth of ZIF-8 Crystals on Non-Polar Surface. *Adv. Mater.* **2012**, *24*, 5954–5958.
29. Yoon, S. M.; Warren, S. C.; Grzybowski, B. A. Storage of Electrical Information in Metal-Organic-Framework Memristors. *Angew. Chem., Int. Ed.* **2014**, *53*, 4437–4441.
30. Prakash, A.; Ouyang, J.; Lin, J. L.; Yang, Y. Polymer Memory Device Based on Conjugated Polymer and Gold Nanoparticles. *J. Appl. Phys.* **2006**, *100*, 054309.
31. Stavila, V.; Talin, A. A.; Allendorf, M. D. MOF-Based Electronic and Opto-Electronic Devices. *Chem. Soc. Rev.* **2014**, *43*, 5994–6010.
32. Lee, J.; Hong, W. G.; Lee, H. Non-Volatile Organic Memory Effect with Thickness Control of the Insulating LiF Charge Trap Layer. *Org. Electron.* **2011**, *12*, 988–992.
33. Kuc, A.; Zibouche, N.; Heine, T. Influence of Quantum Confinement on the Electronic Structure of the Transition Metal Sulfide TS₂. *Phys. Rev. B* **2011**, *83*, 245213.
34. Liu, J. Q.; Zeng, Z. Y.; Cao, X. H.; Lu, G.; Wang, L. H.; Fan, Q. L.; Huang, W.; Zhang, H. Preparation of MoS₂-Polyvinylpyrrolidone Nanocomposites for Flexible Nonvolatile Rewritable Memory Devices with Reduced Graphene Oxide Electrodes. *Small* **2012**, *8*, 3517–3522.
35. Laiho, A.; Majumdar, H. S.; Baral, J. K.; Jansson, F.; Österbacka, R.; Ikkala, O. Tuning the Electrical Switching of Polymer/Fullerene Nanocomposite Thin Film Devices by Control of Morphology. *Appl. Phys. Lett.* **2008**, *93*, 203309.
36. Cui, P.; Lee, J.; Hwang, E.; Lee, H. One-Pot Reduction of Graphene Oxide at Subzero Temperatures. *Chem. Commun.* **2011**, *47*, 12370–12372.
37. Qi, X. Y.; Pu, K. Y.; Li, H.; Zhou, X. Z.; Wu, S. X.; Fan, Q. L.; Liu, B.; Boey, F.; Huang, W.; Zhang, H. Amphiphilic Graphene Composites. *Angew. Chem., Int. Ed.* **2010**, *49*, 9426–9429.
38. Lu, G.; Li, S.; Guo, Z.; Farha, O. K.; Hauser, B. G.; Qi, X.; Wang, Y.; Wang, X.; Han, S.; Liu, X.; et al. Imparting Functionality to a Metal–Organic Framework Material By controlled Nanoparticle Encapsulation. *Nat. Chem.* **2012**, *4*, 310–316.
39. Zhou, X. Z.; Huang, X.; Qi, X. Y.; Wu, S. X.; Xue, C.; Boey, F. Y. C.; Yan, Q. Y.; Chen, P.; Zhang, H. *In Situ* Synthesis of Metal Nanoparticles on Single-Layer Graphene Oxide and Reduced Graphene Oxide Surfaces. *J. Phys. Chem. C* **2009**, *113*, 10842–10846.
40. Shin, H.-J.; Kim, K. K.; Benayad, A.; Yoon, S.-M.; Park, H. K.; Jung, I.-S.; Jin, M. H.; Jeong, H.-K.; Kim, J. M.; Choi, J.-Y.; et al. Efficient Reduction of Graphite Oxide by Sodium Borohydride and Its Effect on Electrical Conductance. *Adv. Funct. Mater.* **2009**, *19*, 1987–1992.
41. Liu, J. Q.; Yin, Z. Y.; Cao, X. H.; Zhao, F.; Wang, L. H.; Huang, W.; Zhang, H. Fabrication of Flexible, All-Reduced Graphene Oxide Non-Volatile Memory Devices. *Adv. Mater.* **2013**, *25*, 233–238.